Bacteriocyte cell death in the pea aphid/*Buchnera* symbiotic system

Pierre Simonet[a,1], Karen Gaget[a], Séverine Balmand[a], Mélanie Ribeiro Lopes[a], Nicolas Parisot[a], Kurt Buhler[b], Gabrielle Duport[a], Veerle Vulsteke[b], Gérard Febvay[a], Abdelaziz Heddi[a], Hubert Charles[a], Patrick Callaerts[b], and Federica Calevro[a,1]

[a]UMR0203, Biologie Fonctionnelle, Insectes et Interactions BF2I, Institut National des Sciences Appliquées (INSA-Lyon), Institut National de la Recherche Agronomique (INRA), University of Lyon, F-69621 Villeurbanne, France; and [b]Laboratory of Behavioral and Developmental Genetics, Department of Human Genetics, Katholieke Universiteit (KU) Leuven, University of Leuven, B-3000 Leuven, Belgium

Edited by Nancy A. Moran, University of Texas at Austin, Austin, TX, and approved January 2, 2018 (received for review November 29, 2017)

Symbiotic associations play a pivotal role in multicellular life by facilitating acquisition of new traits and expanding the ecological capabilities of organisms. In insects that are obligatorily dependent on intracellular bacterial symbionts, novel host cells (bacteriocytes) or organs (bacteriomes) have evolved for harboring beneficial microbial partners. The processes regulating the cellular life cycle of these endosymbiont-bearing cells, such as the cell-death mechanisms controlling their fate and elimination in response to host physiology, are fundamental questions in the biology of symbiosis. Here we report the discovery of a cell-death process involved in the degeneration of bacteriocytes in the hemipteran insect *Acyrthosiphon pisum*. This process is activated progressively throughout aphid adulthood and exhibits morphological features distinct from known cell-death pathways. By combining electron microscopy, immunohistochemistry, and molecular analyses, we demonstrated that the initial event of bacteriocyte cell death is the cytoplasmic accumulation of nonautophagic vacuoles, followed by a sequence of cellular stress responses including the formation of autophagosomes in intervacuolar spaces, activation of reactive oxygen species, and *Buchnera* endosymbiont degradation by the lysosomal system. We showed that this multistep cell-death process originates from the endoplasmic reticulum, an organelle exhibiting a unique reticular network organization spread throughout the entire cytoplasm and surrounding *Buchnera aphidicola* endosymbionts. Our findings provide insights into the cellular and molecular processes that coordinate eukaryotic host and endosymbiont homeostasis and death in a symbiotic system and shed light on previously unknown aspects of bacteriocyte biological functioning.

symbiosis | *Acyrthosiphon pisum* | *Buchnera aphidicola* | bacteriocytes | cell death

Symbiosis is a key source of ecological and evolutionary diversification of eukaryotic organisms throughout the animal and plant kingdoms (1, 2). In a wide variety of insects, symbiotic bacteria are critical determinants of host physiology by complementing incomplete or absent eukaryotic metabolic pathways required for the synthesis of essential nutrients with limited availability in the host diets (3, 4). To sustain their mutually beneficial partnership, host organisms have evolved specialized cells (the bacteriocytes) that can form a symbiosis-dedicated organ (the bacteriome) where obligatory symbiotic bacteria are maintained through vertical transmission across host generations (5, 6). Bacteriocytes are specialized metazoan cells (7) that arose independently in various insect orders, such as Blattodea (8), Coleoptera (9), Diptera (10, 11), Hemiptera (12–16), Hymenoptera (17), and Psocoptera (18). These cells constitute a fascinating riddle in developmental and evolutionary cell biology, as their embryonic origin and the molecular mechanisms governing their development and organogenesis, as well as their death, remain largely unsolved (7, 19–21).

Recent years have seen the pea aphid *Acyrthosiphon pisum*/*Buchnera aphidicola* symbiotic system emerging as a powerful model for studying symbiotic relationships (5, 22–24). In particular, aphid bacteriocytes are a promising system to investigate the molecular and cellular processes controlling bacteriocyte fate for three broad reasons: (*i*) aphid bacteriocytes are giant cells (i.e., a diameter exceeding 100 μm during insect adult life), not structured in specific organs but in weakly adherent cell clusters that can readily be isolated individually for cellular-level analyses; (*ii*) bacteriocyte dynamics have been characterized throughout the aphid life cycle, showing a fine-tuning of these endosymbiont-bearing cells according to the developmental needs of the host (i.e., bacteriocyte structures, coordinately with the *B. aphidicola* endosymbiont population, grow considerably during aphid development, a period in which high nutritional complementation is required, before a progressive decline during adulthood) (25); (*iii*) the genomes of both symbiotic partners have been sequenced and annotated (23, 24), facilitating the analysis of the molecular mechanisms underlying bacteriocyte dynamics.

In the current study, we characterize the cellular mechanisms associated with degeneration and death of bacteriocytes, as well as the removal of endosymbiotic bacteria, in response to aphid development and physiology.

We demonstrate that aphid bacteriocytes degenerate through a hitherto unknown process distinct from evolutionarily conserved pathways, including apoptosis- or autophagy-dependent cell deaths. We show that aphid bacteriocyte cell death is a dynamic process resulting from a progressive hypervacuolation of bacteriocyte

Significance

Beneficial symbiotic associations, ubiquitously found in nature, have led to the emergence of eukaryotic cells, the bacteriocytes, specialized in harboring microbial partners. One of the most fundamental questions concerning these enigmatic cells is how organismal homeostasis controls their elimination. Here we report that aphid bacteriocytes have evolved a form of cell death distinct from the conserved cell-death mechanisms hitherto characterized. This cell-death mechanism is a nonapoptotic multistep process that starts with the hypervacuolation of the endoplasmic reticulum, followed by a cascade of cellular stress responses. Our findings provide a framework to study biological functioning of bacteriocytes and the cellular mechanisms associated with symbiosis and contribute to the understanding of eukaryotic cell-death diversity.

Author contributions: P.S., P.C., and F.C. designed research; P.S., K.G., S.B., M.R.L., K.B., G.D., V.V., P.C., and F.C. performed research; P.S., N.P., G.F., A.H., H.C., P.C., and F.C. analyzed data; and P.S., P.C., and F.C. wrote the paper.

The authors declare no conflict of interest.

This article is a PNAS Direct Submission.

[1]To whom correspondence may be addressed. Email: pierre.simonet@insa-lyon.fr or federica.calevro@insa-lyon.fr.

This article contains supporting information online at www.pnas.org/lookup/suppl/doi:10.1073/pnas.1720237115/-/DCSupplemental.

cytoplasm and that the vacuoles are derived from the endoplasmic reticulum (ER). This in turn triggers a prominent induction of autophagy in the intervacuolar space, a swelling of bacteriocyte mitochondria, and induction of reactive oxygen species (ROS). We interpret these findings as bacteriocyte stress responses induced by the initial cytoplasmic hypervacuolation. Finally, we provide evidence that, in senescent bacteriocytes, the endosymbionts are degraded through a lysosomal-dependent mechanism. These findings define mechanisms by which bacteriocyte cell and symbiont numbers are regulated to maintain organismal homeostasis in a symbiotic insect model. The discovery of a nonapoptotic and nonautophagic cell-death process in an insect model contributes more broadly to the understanding of metazoan cell-death diversity.

Results

Bacteriocyte Degeneration Starts with Cytoplasmic Hypervacuolation. To gain insight into the cellular mechanisms underlying bacteriocyte maturation and degeneration, we performed a detailed morphological analysis of bacteriocyte tissue throughout the pea aphid life cycle. Consistent with previous findings (25), histological analysis revealed a progressive degeneration of bacteriocyte tissue in adult aphids starting at the onset of the reproductive period (Fig. 1). During nymphal development, the bacteriocyte tissue grows considerably and is organized into two regular clusters in close proximity to the aphid gut and the developing embryonic chains (Fig. 1 *A* and *A′*). In contrast, adult aphids exhibit a disorganized architecture of this tissue with a progressive disaggregation that increases with aphid age (Fig. 1 *B* and *C*): Reproductively active adults (A15) start to display disorganized bacteriocyte aggregates in the abdomen (Fig. 1*B′*), and senescent adults (A23) exhibit the strongest degenerative phenotype with the loss of bacteriocyte intercellular adhesion and the appearance of individual disaggregated cells (Fig. 1*C′*). This degenerative phase coincides with the previously described bacteriocyte and endosymbiont cell dynamics in which both host and endosymbiont cell numbers progressively decrease after aphids undergo their final ecdysis and start their laying period (25). The analysis of the cellular morphology confirmed the occurrence of a progressive degenerative process in aging bacteriocytes. Compared with cells in third-instar nymphs (N3) (Fig. 1*D*), degenerative bacteriocytes are characterized by the presence of unstained histological areas that increase in size with age (Fig. 1 *F* and *H*). Although previously designated as "low symbiont-density zones" (25), FISH using *Buchnera*-specific probes demonstrated that these degenerative areas are de facto devoid of primary symbionts (Fig. 1 *G* and *I*). A second change in degenerating bacteriocytes was revealed by fluorescent staining of bacteriocyte DNA and showed that the degeneration process is also associated with alterations of the bacteriocyte nuclear shape. Nuclei, initially round and centrally positioned in bacteriocyte cells during nymphal development (Fig. 1*E*), become progressively deformed and anisotropically oriented at the periphery of the adult cell cytoplasm (Fig. 1 *G* and *I*).

To further characterize the cell-death processes involved in the physiological elimination of bacteriocyte cells, we performed ultrastructural analyses of bacteriocytes throughout the insect life cycle. Remarkably, transmission electron microscopy (TEM) revealed massive cytoplasmic vacuolation in degenerative bacteriocytes (Fig. 2). As apparent from histology and FISH imaging, two major regions can be distinguished in the degenerative bacteriocyte cytoplasm (Fig. 2 *A* and *B*): a peripheral zone filled with thousands of *B. aphidicola* symbionts (Fig. 2*E*) and a central degenerative zone containing numerous large vacuoles (Fig. 2*D* and Fig. S1*A*) ranging from 1 to 10 μm in diameter. Confocal analyses of whole-mount bacteriocytes, doubly stained with fluorescent nuclear (DAPI) and acidotropic (LysoTracker) probes, revealed that the hypervacuolated zone constitutes a large acidic compartment. The degenerative vacuoles first appear in the bacteriocyte cytosol immediately after final ecdysis (A9; young adult) (Fig. S2), concomitant with the start of bacteriocyte elimination at the beginning of aphid adulthood (25). They then rapidly accumulate and progressively expand throughout the entire cell (Fig. S2).

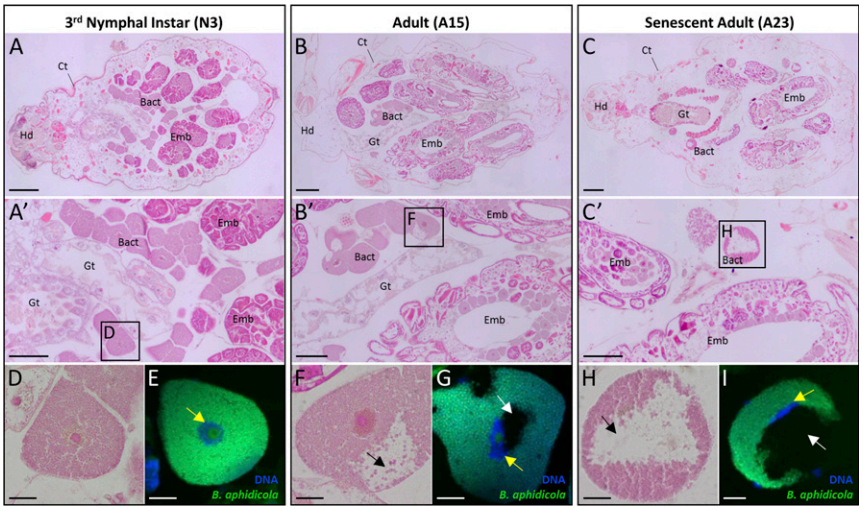

Fig. 1. Degeneration of bacteriocyte tissue and cells during aphid aging. (*A–C*) Representative images of H&E-stained whole-aphid sections from N3 (*A*), reproductively active adults (*B*), and senescent adults (*C*) demonstrating a progressive dissociation of bacteriocyte clusters. (*A′–C′*) Enlarged images of H&E-stained bacteriocyte clusters showing the appearance of disaggregated bacteriocytes and the occurrence of morphological abnormalities with aphid aging. Rectangles correspond to the locations of the following magnified images. (*D*, *F*, and *H*) Magnified views of H&E-stained bacteriocytes. Note the presence of large unstained areas in adult degenerating bacteriocytes (black arrows), previously referred to as "low symbiont-density zones" (25). (*E*, *G*, and *I*) FISH of *B. aphidicola* symbionts (green) and nuclear DNA staining (blue) in bacteriocyte cells demonstrating the absence of symbionts within the low symbiont-density zones (white arrows). Note the progressive changes in bacteriocyte nuclear shape in aphid adults compared with nymphs (yellow arrows). Symbionts or DNA were stained with the Alexa 488-Buch probe specifically targeting *B. aphidicola* 16S rRNA or DAPI, respectively. Bact, bacteriocyte; Ct, cuticle; Emb, embryo; Gt, gut; Hd, head. (Scale bars: 200 μm in *A–C*, 100 μm in *A′–C′*, and 20 μm in *D–I*.)

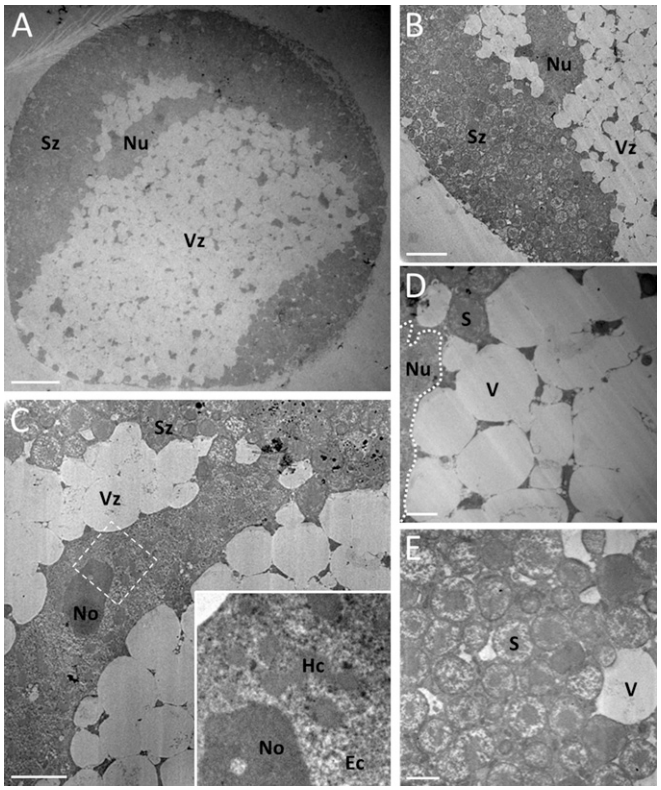

Fig. 2. TEM of *A. pisum* degenerative bacteriocytes. (*A*) Low-magnification image of a degenerative bacteriocyte cell exhibiting extensive cytoplasmic vacuolation and an abnormal nuclear shape. (*B*) Enlarged image of the border between the peripheral cytoplasmic zone filled with *B. aphidicola* symbionts and the central heavily vacuolated zone extending around the nucleus. (*C*) Magnified view of the bacteriocyte nucleus showing loss of its round shape but no major ultrastructural modifications. (*Inset*) Enlarged view of chromatin structures and nucleolus. (Magnification of *Inset*: 6.4-fold.) Note the absence of the characteristic features of apoptosis such as chromatin condensation, nuclear fragmentation, and apoptotic body formation. (*D* and *E*) Magnified images of large cytoplasmic electron-lucent vacuoles (*D*) and *B. aphidicola* symbionts (*E*). Additional high-magnification images of nuclear structures, vacuoles, and symbionts are available in Fig. S1. Ec, euchromatin; Hc, heterochromatin; No, nucleolus; Nu, nucleus; S, symbiont; Sz, symbiont-dense zone; V, vacuole; Vz, vacuole-dense zone. (Scale bars: 20 μm in *A*, 10 μm in *B*, 5 μm in *C*, and 2 μm in *D* and *E*.)

Bacteriocyte Cell Death Is Nonautophagic and Nonapoptotic. Although accumulation of cytoplasmic vacuoles is a feature of autophagic cell death (26, 27), the vacuoles we observed in degenerative bacteriocytes were clearly distinct from autophagosomes or autophagolysosomes. Specifically, vacuoles were electron-lucent and devoid of subcellular components or organelles, attesting to their nonautophagic origin. We also did not observe cell shrinkage, plasma membrane blebbing, or the formation of apoptotic bodies (Fig. 2 *A* and *B*). Furthermore, we found abnormalities in nuclear shape (e.g., lack of uniform circular appearance) in the degenerative bacteriocyte nuclei that, however, did not exhibit the hallmark characteristics of apoptosis (chromatin condensation, nucleolus disorganization, and nuclear fragmentation) (Fig. 2*C* and Fig. S1*B*). The fact that bacteriocyte cell death is not apoptotic in nature was supported by molecular data. Given the extensive functional annotation of the apoptotic pathway in *Drosophila melanogaster* and the relative lack of information in other insects, we used the relevant *Drosophila* proteins to annotate this pathway in *A. pisum*. We then measured the expression profiles of the genes encoding the proteins thus identified in bacteriocytes at different aphid life stages by means of real-time qRT-PCR. Concerning the executive part of the apoptotic pathway, we found *A. pisum* homologs for only four of the eight genes present in *Drosophila*: the genes encoding the adaptor protein Ark, the initiator caspase Dronc, and the two effector caspases (Decay and homologs of the proteins DrICE/Dcp-1) (Fig. S3). For three of these four genes we found two paralogs, resulting in a total of seven apoptotic genes identified. Of these seven genes, three were not expressed in bacteriocyte cells, while the other four were significantly induced during adulthood (between 2.2- and 4.3-fold in A23 senescent adults compared with N3), starting from A15 (Table S1). None was significantly induced between the N3 and A9 life stages, whereas bacteriocyte hypervacuolation was already present at A9. In addition, bacteriocyte gene-expression analyses revealed a significant expression induction (between 3.0- and 6.6-fold in A23 compared with N3) starting from A15 of five (out of seven identified) genes belonging to the inhibitor part of the apoptotic pathway (Fig. S3 and Table S1). The absence of any apoptotic phenotype in TEM images, combined with the late induction of the caspase homologs and the concomitant induction of apoptosis inhibitors, prompted us to classify bacteriocyte degeneration as a nonapoptotic cell death, with the progressive accumulation of nonautophagic vacuoles as one of its hallmarks.

Increased Autophagy During Senescence as a Bacteriocyte Stress Response. Even though the bacteriocyte cytoplasmic hypervacuolation does not result from autophagic cell death, TEM analysis revealed a marked accumulation of autophagic figures separated from the electron-lucent vacuoles (Fig. 3*A*). Abundant and large autophagosomes were formed in intervacuolar spaces, sequestering visible remnants of organelles, as well as membranous whorls (typical autophagic features resulting from the degradation of membranous cellular components). Autophagy is a complex multistep process, genetically regulated by autophagy-related genes (*Atg*). Only a subset of the encoded proteins, referred to as the "core" autophagy machinery, is required for autophagosome formation (28, 29). To further substantiate the activation of autophagy and to determine when autophagy arises relative to other cellular events during bacteriocyte aging, we first completed the Kyoto Encyclopedia of Genes and Genomes (KEGG) annotation of the genes encoding the core ATG proteins in *A. pisum* (Fig. 3*B*) and then measured their expression profiles by means of qRT-PCR. All the homologs of the autophagy pathway are present in the pea aphid genome, and two of these genes (*Atg1* and *Atg3*) underwent duplication. Contrary to apoptotic genes, the expression of all the *Atg* genes was detectable in bacteriocytes at all time points tested here. The mRNA levels of all the *Atg* genes required from phagophore induction to autophagosome formation showed significant age-dependent variations ($P < 0.05$; ANOVA) (Fig. 3*C*). No significant changes in *Atg* gene expression were observed during the growth phase of aphid bacteriocyte tissue (N3–A9), whereas a significant induction occurred during the active period of bacteriocyte degeneration (A9–A23), with 1.8- to 4.4-fold increases in A23 senescent adults compared with N3 [$P < 0.05$; Tukey's highly significant difference (HSD) tests]. Since autophagy, when not promoting cell death, is primarily a protective process for cells maintaining homeostasis under intracellular and extracellular stresses (30, 31), and given that we see increased *Atg* gene expression after the initial signs of vacuolation (A9), we surmise that the elevated autophagy we observed in degenerative bacteriocytes is most likely a stress response to the adverse cellular conditions imposed by the acidic degenerative vacuole accumulation rather than a direct cause of bacteriocyte cell death.

Rearrangement of the Microtubule Network in Senescent Bacteriocytes. We next sought to better define the bacteriocyte subcellular reorganization associated with this nonapoptotic cell death. We initially focused on the microtubules, given their essential role in subcellular organization, in positioning of organelles, and in vesicle

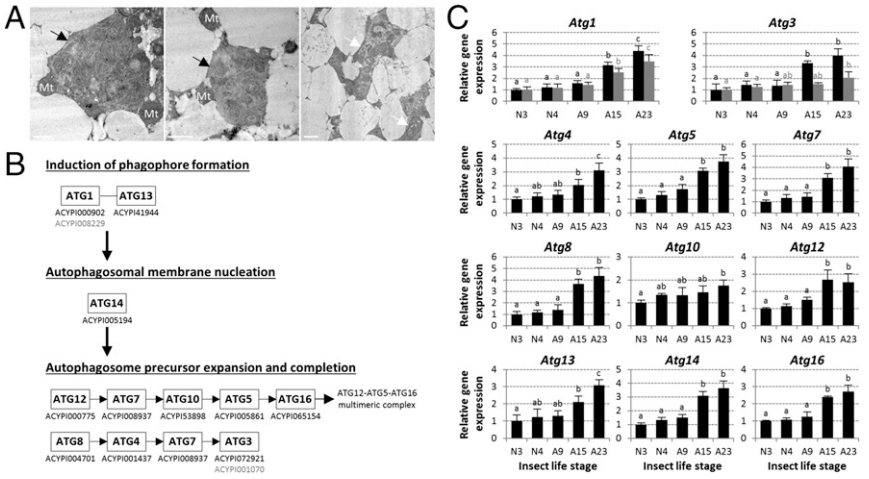

Fig. 3. Activation of autophagy during aphid bacteriocyte degeneration. (*A*) Representative TEM images of autophagic figures accumulating in the intervacuolar space of degenerative bacteriocytes. Black and white arrows denote autophagosomes containing membranous whorls and remnants of cellular organelles, respectively. (Scale bars: 1 μm.) (*B*) Schematic overview of the ATG pathway involved in autophagosome formation in *A. pisum*. Pea aphid ATG homologs are listed with their *A. pisum* (ACYPI) accession number referring to the *A. pisum* genomic database AphidBase (70), and paralogs are shown in different colors (black or gray). (*C*) Induction of *Atg* gene expression in bacteriocyte cells in the course of aphid aging revealed by qRT-PCR. *Atg* gene-expression levels in bacteriocytes at different life stages are expressed relative to the third-instar nymph levels. The *rpl7* gene was used for data normalization. Results are reported as means ± SD (error bars) from three independent experiments. Data were analyzed by one-way ANOVA followed by a post hoc multiple-comparisons test (Tukey's HSD test). Life stages labeled with different letters are significantly different ($P < 0.05$). Paralogs of *Atg1* and *Atg3* genes are displayed in distinct colors (black or gray), according to those used in the ATG pathway (*B*). N3 and N4, third and fourth nymphal stages, respectively; A9, A15, A23, adult time points at days 9, 15, and 23, respectively.

transport. To do so, we developed whole-mount immunohistochemistry for the bacteriocyte cell and examined microtubule organization during bacteriocyte degeneration (Fig. 4). In N3, as assessed by β-tubulin immunostaining, the microtubules organize into a fine, uniform, lace-like network that spans the entire bacteriocyte cytoplasm (Fig. 4*A*). Consistent with the conservation of the general shape of the bacteriocyte, the overall microtubule network of degenerative cells did not display any apparent sign of disorganization (Fig. 4 *B*–*D*). Nevertheless, microtubule rearrangement was observed in the adult bacteriocyte cells, specifically in the heavily vacuolated zones. Compared with the N3 cytoplasm (Fig. 4*E*), these degenerative zones exhibited a dense network characterized by a stronger tubulin-positive signal (Fig. 4 *G*, *I*, and *K*), whereas the symbiont-dense zones did not show any major changes (Fig. 4 *F*, *H*, and *J*). Z-stack analysis and 3D rendering of A15 and A23 adult bacteriocytes (Movies S1–S4) highlighted this heterogeneous organization of microtubules between the two cytoplasmic zones and confirmed that degenerative bacteriocytes do not undergo microtubule rearrangements characteristic of apoptosis [i.e., microtubule depolymerization occurring at the

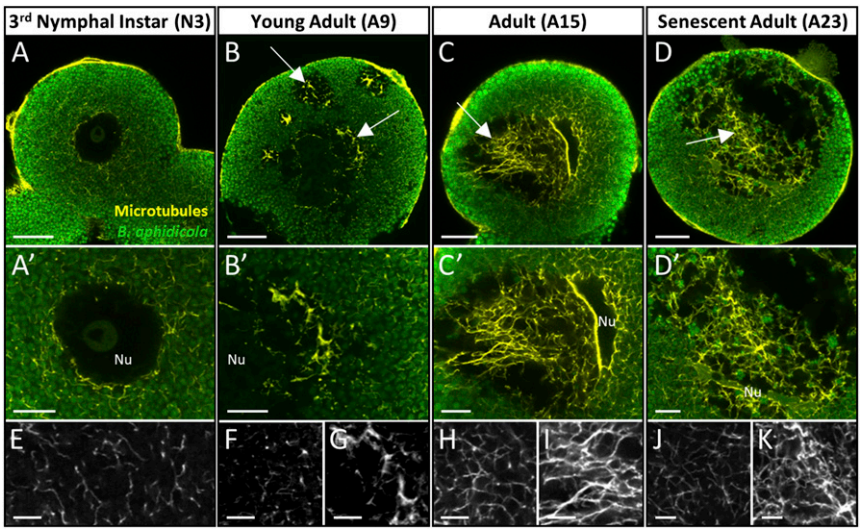

Fig. 4. Organization of the bacteriocyte microtubule network during the degeneration process. (*A*–*D*) Confocal images of the microtubule network (yellow) and *B. aphidicola* symbiont (green) distribution in whole-mount immunohistochemical (IHC)-stained bacteriocytes isolated from N3 (*A*), young adults (*B*), reproductively active adults (*C*), or senescent aphids (*D*). Arrows show a dense microtubule network in the degenerative vacuolated zone. (*A′*–*D′*) Enlarged views of the perinuclear area. (*E*–*K*) Magnified images of the microtubule network in the symbiont-dense zone (*E*, *F*, *H*, and *J*) and vacuole-dense zone (*G*, *I*, and *K*). Aphid symbionts and microtubules were labeled with anti-*Buchnera* GroEL and anti–β-tubulin antibodies, respectively. Z-stack imaging and 3D rotation reconstructions of degenerative bacteriocytes (*C* and *D*) can be observed in Movies S1–S4. Nu, nucleus. (Scale bars: 20 μm in *A*–*D*, 10 μm in *A′*–*D′*, and 5 μm in *E*–*K*.)

early stages of apoptosis, before forming the cortical structure beneath the plasma membrane called the "apoptotic microtubule network," characteristic of the execution phase (32)]. The β-tubulin staining also unequivocally demonstrated that, as bacteriocytes degenerate, the vacuoles accumulate and coalesce, forming larger vacuoles that take up a considerable part of the cytoplasmic volume (Fig. 4*D*, Fig. S4 *A*–*F*, and Movie S4).

ER Origin of Bacteriocyte Degeneration. As hypervacuolated zones of degenerative bacteriocytes developed in close proximity to the nucleus and showed a dense network of microtubules, cytoskeleton components well known to play a fundamental role in regulating ER morphology and distribution (33), we hypothesized that the vacuoles might originate from the ER. To test this, we performed whole-mount immunostaining of bacteriocytes with anti-KDEL antibodies, which specifically target ER-resident and membrane proteins (Fig. 5) (34). Whereas gut control cells exhibit a standard ER morphology, with extended cisternae and a few tubules located in the perinuclear region and periphery of cells, respectively (Fig. 5*A*), bacteriocytes show a radically different ER organization (Fig. 5*B*). Bacteriocyte ER is not constituted of flattened cisternal sheets but distributes as a continuous reticular network composed of densely interconnected structures that extend throughout the entire cytoplasm surrounding *B. aphidicola* endosymbionts. Interestingly, analyses of degenerative bacteriocyte cells revealed maintenance of this ER organization in the symbiont-dense zone and, more importantly, the presence of $KDEL^+$ signals in the hypervacuolated zone (Fig. 5 *C*–*E*). Consistent with this finding, we observed by TEM that intervacuolar spaces contained typical ER structures from which nascent vacuoles were budding (Fig. 5*F*). We also noticed that the cytosolic face of degenerative vacuoles was often studded with ribosomes (Fig. 5*G*), a typical feature of ER membranes, and was close to swollen mitochondria (Fig. 5*H*). During this late phase, we occasionally observe extranuclear chromatin (Fig. S4 *G* and *H*) that could potentially be due to the fusion of acidic ER-derived vacuoles with the bacteriocyte nucleus. Finally, we also demonstrated increased production of intracellular ROS in degenerative bacteriocytes (A15), after the onset of ER-derived hypervacuolation (A9) (Fig. S5).

Symbiont Degradation Through the Activation of the Lysosomal System. Since we identified the ER-derived vacuoles as acidic compartments (Fig. S2), we next asked whether the vacuoles were positive for the late endosomal and lysosomal marker RAB7 (35). Whole-mount immunohistochemistry experiments revealed an age-dependent progressive accumulation of $RAB7^+$ vesicles (Fig. 6 *A*–*E*). Interestingly, these endo-lysosomal vesicles were never detected in the hypervacuolated zone but were in the peripheral symbiont-dense zone instead. Dual labeling with specific *B. aphidicola* antibodies and TEM analysis clearly showed that $RAB7^+$ membranes enclosed aphid primary endosymbionts, which were then degraded inside these vesicles (Fig. 6 *E′* and *G* and Fig. S1 *E* and *F*). This massive endosymbiont degradation appeared to arise essentially in the late phase of bacteriocyte degeneration, with 203 ± 70 $RAB7^+$ *B. aphidicola*-enclosing vesicles quantified per confocal section (n = 25) in senescent adults (A23), against only 5 ± 4 and 9 ± 5 vesicles in A9 and A15 aphid life stages, respectively. We confirmed the involvement of the lysosomal system by analyzing the expression profiles of 17 genes coding for proteins implicated in the major lysosomal activities (Fig. 6*F* and Fig. S6). qRT-PCR analyses revealed significantly up-regulated expression of 13 of these 17 genes in A23 aphids compared with A9. Of these 13, 10 were already significantly up-regulated at A15 compared with A9 ($P < 0.05$; Tukey's HSD tests).

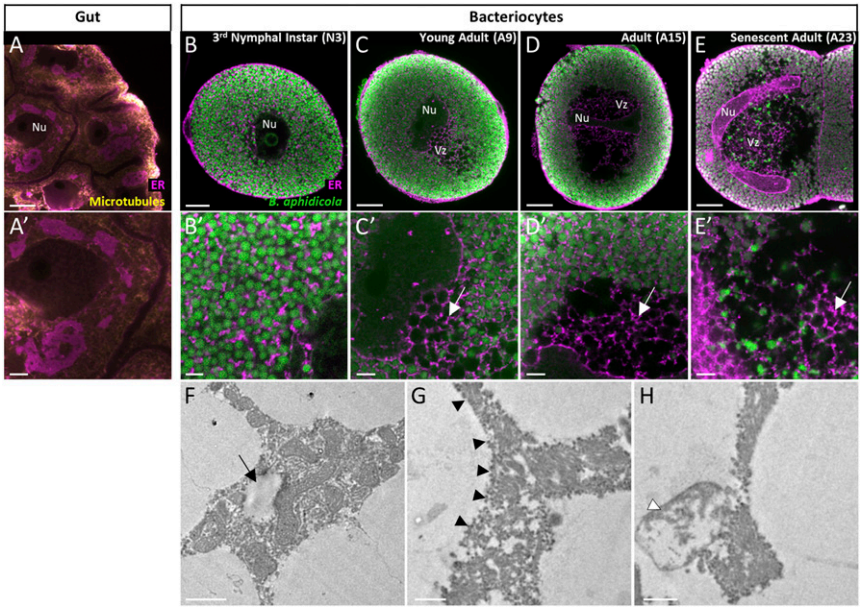

Fig. 5. ER-derived origin of hypervacuolation in degenerative bacteriocytes. (*A*–*E′*) Confocal images (*A*–*E*) and magnified views of ER organization (*A′*–*E′*) in whole-mount IHC-stained gut (controls; *A* and *A′*) and bacteriocytes from N3 (*B* and *B′*), young adults (*C* and *C′*), reproductively active adults (*D* and *D′*), and senescent aphids (*E* and *E′*). ER (magenta), microtubule network (yellow), and *B. aphidicola* symbionts (green) were labeled with anti-KDEL, anti–β-tubulin, or anti-*Buchnera* GroEL antibodies, respectively. White arrows show the ER^+ labeling in the degenerative bacteriocyte vacuolated zone. Note the discrepancy of ER organization between gut and bacteriocyte cells, with structured in cisternae around nuclei in the gut or forming a reticular network enveloping symbionts in bacteriocytes. Z-stack imaging and 3D rotation reconstructions of degenerative bacteriocytes (*D* and *E*) can be observed in Movies S5–S8. (*F*–*H*) Representative TEM images of intervacuolar spaces in degenerative bacteriocytes revealing the ER origin of vacuoles. The black arrow shows a nascent vacuole originating from ER. Black and white arrowheads denote ribosomes that label the cytosolic face of the vacuole membrane and swollen mitochondria, respectively. Nu, nucleus; Vz, vacuole-dense zone. (Scale bars: 20 μm in *A*–*E*, 5 μm in *A′*–*E′*, 1 μm in *F*, and 0.5 μm in *G* and *H*.)

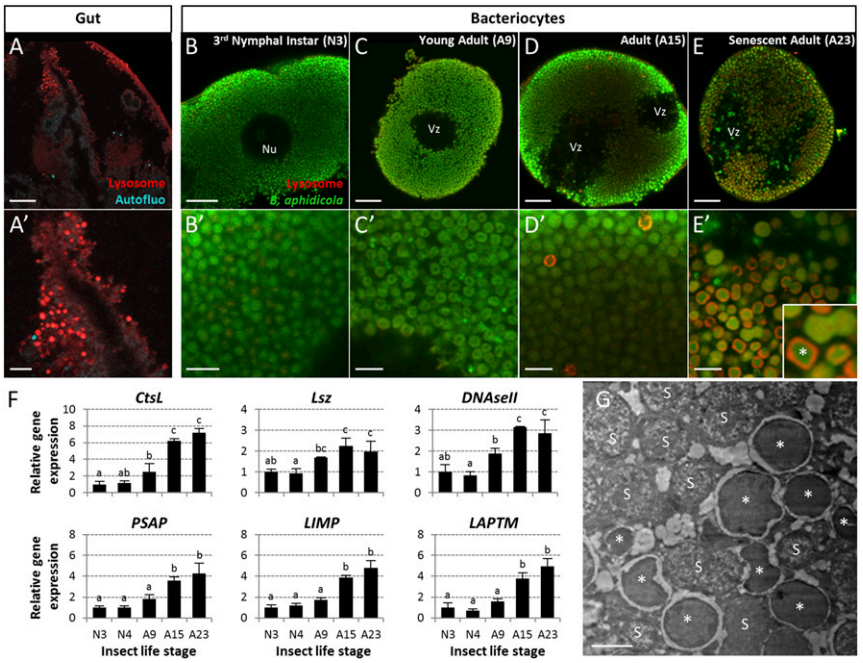

Fig. 6. Activation of the lysosomal system during aphid bacteriocyte degeneration. (*A*–*E*′) Confocal images (*A*–*E*) and magnified views (*A*′–*E*′) of lysosomes in whole-mount IHC-stained gut (controls; *A* and *A*′) and bacteriocytes from N3 (*B* and *B*′), young adults (*C* and *C*′), reproductively active adults (*D* and *D*′), and senescent aphids (*E* and *E*′). *B. aphidicola* symbionts (green) and lysosomes (red) were labeled with anti-*Buchnera* GroEL and anti-RAB7 antibodies, respectively. (*E*, *Inset*) Enlarged image of the lysosomal membrane enclosing a *B. aphidicola* symbiont. *B. aphidicola* symbionts (asterisk) engulfed in lysosomes in degenerative bacteriocytes. (Magnification of *Inset*: 5.3-fold.) Note the presence in degenerative bacteriocytes (*D* and *E*) of lysosome-positive signals only in symbiont-dense zones and not in vacuole-dense zones. Nu, nucleus; Vz, vacuole-dense zone. (Scale bars: 20 μm in *A*–*E*, and 5 μm in *A*′–*E*′′.) (*F*) Induction of lysosomal gene expression in bacteriocytes throughout aphid aging as revealed by qRT-PCR. Expression profiles of representative genes for major lysosomal activities: lysosomal acid hydrolases (*CtsL*), glycosidases (*Lsz*), and nucleases (*DNaseII*); activators (*PSAP*); or major (*LIMP*) and minor (*LAPTM*) membrane proteins (for a comprehensive overview of lysosomal gene-expression analysis, see Fig. S6). Gene-expression levels in bacteriocytes at different life stages are expressed relative to the third-instar nymph level. The *rpl7* gene was used for data normalization. Results are reported as means ± SD (error bars) from three independent experiments. Data were analyzed by one-way ANOVA followed by a post hoc multiple-comparisons test (Tukey's HSD test). Life stages labeled with different letters are significantly different ($P < 0.05$). Gene names: *CtsL*, *cathepsin-L*; *DNaseII*, *DNase II*; *LAPTM*, *lysosomal-associated protein transmembrane*; *LIMP*, *lysosomal integral membrane protein*; *Lsz*, *lysozyme i-1; PSAP*, *prosaposin*. A9, A15, A23, adult time points at days 9, 15, and 23, respectively; N3 and N4, third and fourth nymphal stages, respectively. (*G*) Representative TEM image of lysosomes containing *B. aphidicola* symbionts (asterisks) in degenerative bacteriocytes. Unaffected symbionts are marked with an "S." Additional high-magnification images are available in Fig. S1. (Scale bar: 2 μm.)

Discussion

In multicellular organisms, cell-death processes play a fundamental role in development and organismal homeostasis, physiologically controlling the number and the organization of cells in tissues and organs (36). Although apoptosis- and autophagy-dependent cell deaths are the most prominent and best-studied in metazoan cells, recent studies have identified various alternative mechanisms (37–45), so far restricted to mammalian cells. In the present study, we have discovered a form of cell death involved in the physiological degeneration of insect bacteriocytes during aphid aging. We also describe the unique organization of the ER in these cells and its crucial role in bacteriocyte cell death.

Compared with the apoptotic and nonapoptotic mechanisms hitherto characterized, the process in aphid bacteriocytes displays a unique combination of cell-death features (summarized in Table S2). After an important phase of growth throughout aphid development (25), bacteriocytes are progressively eliminated during insect adulthood through a degenerative process that starts with an extensive ER-derived hypervacuolation of cytoplasm and which is clearly distinct from apoptosis at morphological and molecular levels. Specifically, bacteriocyte cell death does not show cell shrinkage, plasma membrane blebbing, formation of apoptotic bodies, chromatin condensation, or nuclear fragmentation (Table S2). Furthermore, we observed, on the one hand, increased expression of four proapoptotic genes in bacteriocytes of senescent aphids (A23) and, on the other hand, a simultaneous significantly increased expression of five apoptosis-inhibitor genes. We interpret these molecular data as a possible mechanistic explanation for the absence of morphological signatures for apoptosis, i.e. the blocking of apoptosis in late stages by means of apoptosis inhibitors. Although different forms of nonapoptotic cell death, like paraptosis (37), necroptosis (42), or oncosis (45), have been previously reported to result in an accumulation of cytoplasmic vacuoles originating from swollen ER, especially following in vitro treatments or in in vivo pathological conditions, the ultrastructural changes observed in the physiological bacteriocyte degeneration are distinct. Contrary to paraptosis (37) or necroptosis (42), bacteriocyte cell death does not cause any observable swelling of perinuclear space or dilation of the nuclear membrane resulting in a "balloon-like" nuclear morphology concomitant with ER expansion. Furthermore, whereas oncotic cell death leads to nuclear chromatin clumping (45), the degenerative bacteriocyte nuclei do not undergo such ultrastructural modifications. They do, however, show changes in shape, possibly being compressed by the surrounding ER-derived vacuoles.

Besides the identification of the ER-derived hypervacuolation as the starting point of bacteriocyte cell death, our results indicate that bacteriocyte degeneration also involves the activation of cellular stress responses, all following bacteriocyte hypervacuolation, in a stepwise manner (Fig. 7). After the initiation of vacuole formation, mitochondrial swelling occurs not at random cellular locations but specifically in the heavily vacuolated zones. Given the exquisite sensitivity of mitochondria to metabolic shifts in

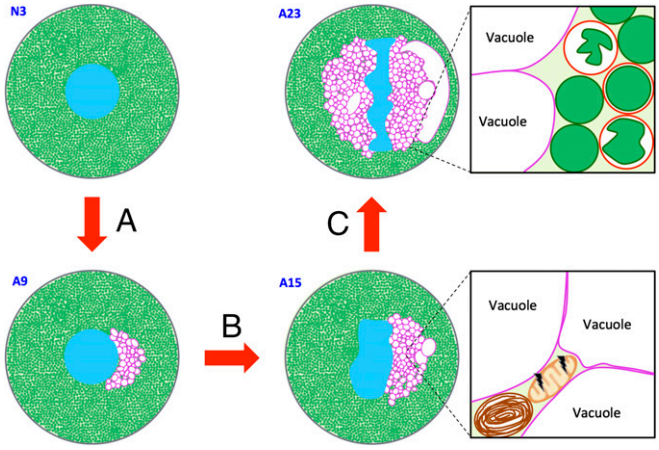

Fig. 7. Major phases of aphid bacteriocyte cell death. (*A*) Phase I: induction of ER-derived hypervacuolation. (*B*) Phase II: induction of bacteriocyte stress responses (autophagy activation and mitochondria swelling in the intervacuolar spaces). (*C*) Phase III: lysosome-mediated degradation of *Buchnera*. Blue, bacteriocyte nucleus; brown, autophagosome; dark green, *B. aphidicola*; light green, bacteriocyte cytoplasm; magenta, ER-derived vacuole membranes; peach, mitochondria; red, lysosomes.

water and electrolyte balance, oxygen tension, or pH, we hypothesize that the mitochondrial phenotype is due to adverse metabolic conditions in the hypervacuolated zones, possibly imposed by the acidosis of this degenerative area (Fig. S2). Furthermore, as in most metazoan apoptotic (26) or nonapoptotic cell deaths (42, 44, 46, 47), aphid bacteriocyte degeneration is associated with increased levels of intracellular ROS. Because the production of these oxidant species did not precede the initiation of bacteriocyte cell death, we also interpret this as a cellular stress response activated concomitantly with mitochondrial dysfunction. In parallel, the bacteriocyte autophagic machinery is activated with a significant induction of *Atg* genes, leading to the formation of autophagosomes sequestering damaged organelles. It should be emphasized that, similarly to the mitochondrial swelling, the autophagic figures are not formed randomly within bacteriocytes but are located specifically in the intervacuolar spaces. As autophagy exerts a primordial prosurvival function in the setting of most forms of cellular stress, including nutrient and growth factor deprivation, protein accumulation, or, noticeably, ER stress, the activation of the bacteriocyte autophagic process might be a protective mechanism to maintain cellular homeostasis in response to ER-derived degeneration via the elimination and recycling of defective organelles. Over the last decade a series of studies has shown that the ER constitutes a source of autophagosomal membranes and also functions as an inducer of autophagy to overcome associated stresses (48, 49), thus supporting the hypothesis that initial ER-derived hypervacuolation triggers the autophagic response in bacteriocyte cell death.

At the last steps of bacteriocyte degeneration, potent lysosomal activity is induced. Thus, far, only one study has reported high expression levels of the lysosomal *lysozyme i-1* homolog in pea aphid bacteriocytes at advanced adult stages (corresponding to aphid life stages A15–A23 analyzed here) (50). Our results comprise expression analysis of 17 lysosomal genes. They also define the dynamics of lysosomal activation over time, quantify its extent, and clearly demonstrate the occurrence of a massive degradation of endosymbionts engulfed in lysosomal structures. This progressive activation of the lysosomal system could be a mechanism to reduce the physiological costs of maintaining the symbionts in degenerative cells and also to recycle *B. aphidicola*. Furthermore, the fact that RAB7^{+} lysosomes appear only in senescent aphids is particularly intriguing in light of studies in different coral species (e.g., *Aiptasia pulchella* and *Acropora digitifera*). These corals harbor endosymbiotic dinoflagellates in the so-called "symbiosome" that arises through phagocytosis and is likely similar in function and origin to the symbiosomal structure containing *B. aphidicola* in aphid bacteriocytes (51–54). The symbiosome in these corals is described as an arrested phagosome, which evades maturation at the early phases of symbiosis establishment and functioning by recruitment of different RAB proteins and excludes RAB7 (54). The recruitment of RAB7 proteins and the progression of the endosymbiont-containing phagosomes to lysosomes occur only at late stages of the coral life cycle, before the degeneration of the host cell by cell death. Further molecular studies will be needed to understand whether endosymbionts in the *A. pisum*/*B. aphidicola* symbiotic system evade lysosomal degradation by manipulating the endomembrane system at the early steps of symbiosis establishment, before the activation of bacteriocyte cell death.

Recent investigations on *Sitophilus* weevils, a coleopteran species symbiotically associated with the *Sodalis pierantonius* bacterium, have revealed a distinct mechanism of bacteriocyte degeneration (21). In this recently established symbiosis (dating to less than 0.03 My) (55), weevil bacteriomes associated with the gut are totally and rapidly eliminated in young adults by a combination of apoptosis and autophagy (21). Autophagy has also been identified as a regulatory mechanism to control intracellular pathogens or parasitic reproductive endosymbionts (56). The nonapoptotic type of cell death observed in aphid bacteriocytes might be a consequence of the long coevolutionary history of aphids with *B. aphidicola* (up to 150 My) (57). Contrary to *S. pierantonius*, *B. aphidicola* endosymbionts have suffered extreme genome shrinkage (23, 58), functionally specializing in aphid nutritional complementation and not retaining immunogenic factors that could induce apoptosis in infected cells, such as the type III secretion system (59, 60). Furthermore, the long-lasting symbiosis with *B. aphidicola* in aphids led to a very high level of integration of these symbionts in the physiology of their hemipteran hosts, rendering them profitable throughout the whole aphid life cycle and thus resulting in the maintenance of a finely regulated number in aging aphids matching host physiological demand (25). In contrast to weevils, aphids maintain their endosymbionts throughout adulthood and eliminate them during their aging as a part of a stepwise bacteriocyte cell-death process. Given that bacteriocytes evolved independently in many different insect orders, it remains to be seen whether the bacteriocyte cell death identified in the present study is a conserved mechanism across insects or is restricted to species with evolutionary ancient symbiosis such as aphids and other hemipteran species.

While characterizing aphid bacteriocyte cell death, we discovered the unique organization of the ER in a continuous reticular network spread through the entire cytoplasm. This configuration is distinct from the standard ER organization we observed in the gut. We propose that this intriguing disposition might confer functional advantages to both the host cells and the endosymbionts. On the one hand, the reticular distribution of the ER may guarantee its biosynthetic and transport functions throughout the cell despite its being loaded with endosymbionts. On the other hand, since the *B. aphidicola* symbionts are dependent on aphid metabolism for the biosynthesis of 18 amino acids (being auxotrophic for eight of them, the nonessential alanine, asparagine, aspartate, glutamate, glutamine, proline, serine, and tyrosine) (22, 23), as a result of extensive genome shrinkage, the close proximity of the ER with each endosymbiont could endow the bacteria with a metabolic advantage important for their survival and for the endosymbiotic relationship.

Conclusion

Taken together, the discovery of a unique ER organization and cell-death mechanism in aphid bacteriocytes sheds light on specialized endosymbiont-bearing cells in insects with long-lasting

symbiotic relationships. Future challenges will be (*i*) to determine whether and how *B. aphidicola* manipulates the host bacteriocyte to allow its own expansion (e.g., using ER subversion strategies similar to those used by pathogenic bacteria) (61), (*ii*) to identify potential *B. aphidicola* inducers of bacteriocyte cell death, (*iii*) to identify eukaryotic regulators [e.g., effectors such as the newly discovered BCRs that could be involved in the regulation of endosymbiont numbers (62) in the aphid bacteriocyte degenerative process], and (*iv*) to characterize how bacteriocyte life and death are integrated in and regulated by host physiology. In a broader context, this study reveals the existence in an insect model of a cell-death process distinct from apoptotic and autophagic cell death. Whether this is unique to aphid bacteriocytes is an intriguing issue in evolutionary cell biology, which could be addressed by comparative genomic and functional studies of cell-death pathways in symbiotic and nonsymbiotic insects.

Materials and Methods

Biological Materials. Aphids used in this study were obtained from a long-established parthenogenetic clone (LL01) of *A. pisum* Harris containing only the primary endosymbiont *B. aphidicola*. The absence of any of the secondary symbionts regularly occurring in pea aphids [i.e., *Hamiltonella defensa*, PAXS (Pea Aphid X-type Symbiont), *Regiella insecticola*, *Rickettsia* sp., *Rickettsiella* sp., *Serratia symbiotica*, and *Spiroplasma* sp.] was checked by using the PCR-based diagnostic described by Peccoud et al. (63). All insects were developmentally synchronized, as previously described (25), and were reared on young broad bean plants (*Vicia faba* L. cv. Aguadulce) at 21 °C, with a photoperiod of 16 h light/8 h dark, maintaining aphids as strictly parthenogenetic matrilines.

For all experiments, aphids were collected at different life stages: nymphs at N3 (third instar; 5 d old) or N4 (fourth instar; 7 d old); reproductive adults at A9 (9 d old) or A15 (15 d old); and senescent adults at A23 (23 d old) during the aphid aging period. Bacteriocytes or gut were surgically isolated from the aphid abdomen in ice-cold isosmotic buffer A (0.025 M KCl, 0.01 M $MgCl_2$, 0.25 M sucrose, and 0.035 M Tris·HCl, pH 7.5) under 25×–40× magnification with a MDG-17 stereomicroscope (Leica) and were collected with a Pasteur glass pipette attached to a vacuum pump or with fine forceps (Dumont no. 5), respectively.

Antibodies. For whole-mount immunohistochemistry, the following primary antibodies were used: rabbit anti-*Buchnera* GroEL [produced and supplied by H. Ishikawa's laboratory (64); 1:200 dilution], rat anti-KDEL (no. 50601; 1:200 dilution; Abcam), mouse anti-RAB7 (no. 50533; 1:200 dilution; Abcam), and mouse anti–β-tubulin [E7; 1:10 dilution; Developmental Studies Hybridoma Bank at the University of Iowa (DSHB)]. Species-specific mouse/rabbit/rat secondary antibodies conjugated to FITC, Cy3, or Cy5 (1:200 dilution; Jackson ImmunoResearch) were used.

For immunoblot analyses, rat anti-KDEL (1:3,000 dilution), mouse anti-RAB7 (1:2,000 dilution), and mouse anti–β-tubulin (1:200 dilution) primary antibodies and species-specific secondary antibodies conjugated to HRP (1:3,000 dilution; Jackson ImmunoResearch) were used.

Antibody reactivity with aphid proteins was validated in Western blot and immunostaining experiments (Fig. S7).

Aphid Section Preparation. For histological staining or FISH of nymph and adult sections, appropriately staged aphids were fixed at 4 °C for at least 24 h in PBS with 4% paraformaldehyde or 4% paraformaldehyde and 1% Triton X-100, respectively. After several washes in PBS, samples were stained in 1% eosin for 1 min and embedded in 1.3% agar to facilitate manipulation. Afterward, samples were dehydrated through a series of ascending ethanol solutions, from 70% to absolute ethanol, and were then moved to 1-butanol at 4 °C for 1 d. Next, aphids were embedded in Paraplast (McCormick Scientific LLC) and sectioned at 3-μm thickness using a HM340E electronic rotary microtome. Sections were placed on polylysine-coated slides and conserved at 4 °C until staining.

Histology. Sections were deparaffinated in methylcyclohexane and rehydrated through an ethanol series to PBS. H&E staining was performed using RAL products (RAL Diagnostics) as previously described (65), and sections were mounted with Mountex mounting medium (Histolab). Observations were performed under transmitted light using an inverted IX81 Olympus microscope (Olympus Corporation). Images were captured using an Olympus XM10 CCD gray-scale camera linked to the CellF software (Soft Imaging 197 System).

FISH. Deparaffinated sections were permeabilized in 70% acetic acid at 60 °C for 1 min. After sections were dehydrated through a series of ascending ethanol solutions and air-dried, deproteinization was performed in hydrochloride acid (0.01 M) with pepsin (0.1 mg/mL) at 37 °C for 10 min. Prehybridization was then carried out at 45 °C for 30 min in prehybridization buffer [79% of hybridization buffer (0.9 M NaCl, 20 mM Tris, 5 mM EDTA, pH 7.2), 20% Denhardt's solution (5 g Ficoll, 5 g polyvinylpyrrolidone, 5 g BSA, in 500 mL of water), and 1% SDS solution (SDS 10%)]. In situ hybridization was performed by coating slides at 45 °C for 3 h, protected from light, with an oligonucleotide probe specifically targeting *B. aphidicola* 16S rRNA, whose 5′ end was labeled with Alexa Fluor 488 (10 μg/mL in hybridization buffer) (Table S3). Sections were mounted in PermaFluor Aqueous Mounting Medium (Thermo Fisher Scientific) with DAPI (3 μg/mL; Vector Laboratories). Positive fluorescent signals were analyzed with the epifluorescence IX81 Olympus microscope equipped with appropriate emission filters: HQ535/50 and D470/40 for green and blue signals, respectively.

TEM. Freshly collected bacteriocytes were fixed with 3% glutaraldehyde in sodium cacodylate buffer (0.1 M) for 48 h at 4 °C and were postfixed in 1% osmium tetroxide for 60 min. Samples were dehydrated through a graded ethanol series and then were incubated in a mix of absolute ethanol/propylene oxide (vol/vol) for 2 h. Bacteriocytes were embedded in Epon 828 (Merck KGaA) with 1.7% benzyl dimethyl amine (BDMA) at 60 °C for 72 h. From the resulting resin blocks, 70-nm-thick sections were cut using an EM UC7 Ultramicrotome (Leica) and were placed on 100-mesh copper grids (the minimum size allowing whole-bacteriocyte visualization). Ultrathin sections were contrasted with Uranyless (Delta Microscopies) at 25 °C for 4 min and then with lead citrate at 20 °C for 4 min using a Reichert Ultrostainer (Leica) and were observed with a CM120 transmission electron microscope (Philips).

Whole-Mount Immunohistochemistry. Whole-mount immunostaining of aphid bacteriocytes or guts was performed with a technique modified from Clements et al. (66). Freshly collected bacteriocytes or guts were individually transferred into 96-well or 12-well cell-culture plates, respectively, fixed in ice-cold 3.7% formaldehyde for 30 min, and then preincubated in PAXD-Tween 20 [1× PBS containing 5% BSA, 0.3% Tween 20 and 0.3% sodium deoxycholate] for at least 15 min. Aphid tissues were then sequentially incubated with primary and secondary antibodies in PAXD-Tween 20 overnight at 4 °C, protected from light. Stained tissues were mounted on glass slides in VECTASHIELD mounting medium (Vector Laboratories) with DAPI, using spacers cut from coverslips to avoid crushing the cells. Throughout the process, staining and washing solutions were removed with an extra thinly pulled Pasteur glass pipette attached to a vacuum pump. For bacteriocytes, this solution-removal step was always performed under a MDG-17 stereomicroscope to check the integrity of cells and to keep them in the smallest volume possible. Confocal images were collected as single optical sections or Z-series (serial optical sections at 0.1-μm intervals) using a Fluoview FV1000 confocal microscope (Olympus Corporation). Confocal 2D images, Z-slice movies, and 3D reconstructions were processed with ImageJ software (67).

LysoTracker Staining. Freshly collected bacteriocytes were individually transferred into 96-well cell-culture plates and incubated in the dark for 60 min at 4 °C with 100 nM LysoTracker Yellow HCK-123 (Invitrogen) in buffer A. After thoroughly washing in buffer A, bacteriocytes were incubated with 3 μg/mL DAPI in buffer A for 5 min at room temperature before mounting on glass slides using spacers cut from coverslips. DAPI and LysoTracker-positive signals were analyzed with a Fluoview FV1000 confocal microscope.

Detection of Intracellular ROS. Freshly collected bacteriocytes were individually transferred into 96-well cell-culture plates and incubated in the dark for 30 min at 4 °C with 10 μM 2′,7′-dichlorodihydrofluorescein diacetate (H_2DCFDA; Thermo Fisher Scientific) in buffer A following a protocol adapted from Mangano et al. (68). After several washing steps in buffer A, bacteriocytes were fixed in PBS with 4% paraformaldehyde. Stained cells were mounted in PermaFluor Aqueous Mounting Medium with DAPI (3 μg/mL) and analyzed with fluorescence microscopy using the IX81 Olympus microscope. Images were captured under a constant gain and exposure time using an F-view camera linked to the CellF software, and ROS were quantified with ImageJ software (67).

Immunoblotting. Fifteen aphids (from a mix of distinct nymphal and adult life stages) were pooled, washed with PBS, and gently crushed in cell lysis buffer (MCL1-1KT; Sigma-Aldrich) supplemented with protease inhibitor mixture (Roche). Aphid tissue lysate was incubated on ice for 15 min and then centrifuged (12,000 × *g*, 5 min, 4 °C). The supernatant was used for immunoblotting, and its protein concentration was determined using the Bio-Rad Protein assay (Bio-Rad Laboratories). Twenty micrograms of protein were separated on Bolt 4–12% Bis-Tris Plus gels (Thermo Fisher Scientific) using Bolt Mes SDS running buffer and were blotted onto a nitrocellulose membrane. Membranes were blocked with Western Blocking Reagent (Roche) and probed with primary antibodies. Immunodetection was performed with HRP-conjugated secondary antibodies and the ECL-Plus chemiluminescent detection system (Amersham Biosciences).

qRT-PCR. Total RNA was extracted from freshly collected bacteriocytes of 30 aphids using the RNeasy Mini Kit (Qiagen). The RNA was treated with DNase I (Promega), and first-strand cDNA was synthetized using the SuperScript III First-Strand Synthesis System (Invitrogen) with oligo(dT)20 primers (Thermo Fisher Scientific). Real-time RT-PCR reactions were performed on a LightCycler 480 instrument (Roche) using 1:5-diluted cDNAs and SYBR Green PCR Master mix according to the manufacturer's instructions. mRNA levels were quantified relative to the constitutively expressed *rpl7* (*ACYPI010200*) gene that was retained by the BestKeeper software tool (69) as the best normalization gene compared with other candidates: *actin* (*ACYPI000064*) and *rpl32* (*ACYPI000074*). Primers used in this study are listed in Table S3. The expected PCR amplicon sizes and sequences were controlled by gel electrophoresis and Sanger sequencing. For each analyzed aphid life stage, three independent biological replicates were processed (each biological replicate was composed of total RNA extracted from a bacteriocyte collection of 30 aphids). All qRT-PCR reactions were performed in technical triplicates, and relative expression levels were calculated as previously described (65).

Statistics. Data normality and homoscedasticity assumptions were checked with the Shapiro–Wilk and Bartlett tests, respectively. Experimental data were analyzed by ANOVA followed by post hoc multiple comparisons using Tukey's HSD test. All statistical analyses were carried out using R software v3.1.1 with values of $P < 0.05$ considered significant. Throughout the paper, results are displayed as means ± SD of three independent biological experiments.

ACKNOWLEDGMENTS. We thank Melissa Beelen and Alain Clavel for plant production, Akiko Sugio for her kind donation of the Alexa488-Buch probe specifically targeting *B. aphidicola* 16S rRNA, Catherine Fiol and Lionel Razy for logistical support, and Elyane Chassignol for secretarial assistance. qRT-PCR experiments were performed at Développement de Techniques et Analyse Moléculaire de la Biodiversité, and electron microscopy and confocal observation were done at CTμ, two platforms of the Fédération de Recherche Bio-Environnement et Santé of the University of Lyon. This work was supported by the Institut National des Sciences Appliquées-Lyon, Institut National de la Recherche Agronomique, and French National Research Agency Program Grant ANR-13-BSV7-0016-03 (Immune and Metabolic Control in Intracellular Symbiosis of Insects; IMetSym). P.S. and M.R.L. were awarded PhD fellowships by the French Ministry of Research.

1. Gilbert SF, Sapp J, Tauber AI (2012) A symbiotic view of life: We have never been individuals. *Q Rev Biol* 87:325–341.
2. McFall-Ngai M, et al. (2013) Animals in a bacterial world, a new imperative for the life sciences. *Proc Natl Acad Sci USA* 110:3229–3236.
3. McCutcheon JP, von Dohlen CD (2011) An interdependent metabolic patchwork in the nested symbiosis of mealybugs. *Curr Biol* 21:1366–1372.
4. Wilson AC, Duncan RP (2015) Signatures of host/symbiont genome coevolution in insect nutritional endosymbioses. *Proc Natl Acad Sci USA* 112:10255–10261.
5. Koga R, Meng XY, Tsuchida T, Fukatsu T (2012) Cellular mechanism for selective vertical transmission of an obligate insect symbiont at the bacteriocyte-embryo interface. *Proc Natl Acad Sci USA* 109:E1230–E1237.
6. Luan JB, et al. (2016) Cellular and molecular remodelling of a host cell for vertical transmission of bacterial symbionts. *Proc Biol Sci* 283:20160580.
7. Matsuura Y, Kikuchi Y, Miura T, Fukatsu T (2015) Ultrabithorax is essential for bacteriocyte development. *Proc Natl Acad Sci USA* 112:9376–9381.
8. López-Sánchez MJ, et al. (2009) Evolutionary convergence and nitrogen metabolism in *Blattabacterium* strain Bge, primary endosymbiont of the cockroach *Blattella germanica*. *PLoS Genet* 5:e1000721.
9. Login FH, et al. (2011) Antimicrobial peptides keep insect endosymbionts under control. *Science* 334:362–365.
10. Hosokawa T, et al. (2012) Reductive genome evolution, host-symbiont co-speciation and uterine transmission of endosymbiotic bacteria in bat flies. *ISME J* 6:577–587.
11. International Glossina Genome Initiative (2014) Genome sequence of the tsetse fly (*Glossina morsitans*): Vector of African trypanosomiasis. *Science* 344:380–386.
12. Nakabachi A, et al. (2006) The 160-kilobase genome of the bacterial endosymbiont *Carsonella*. *Science* 314:267.
13. Gottlieb Y, et al. (2008) Inherited intracellular ecosystem: Symbiotic bacteria share bacteriocytes in whiteflies. *FASEB J* 22:2591–2599.
14. Hosokawa T, Koga R, Kikuchi Y, Meng XY, Fukatsu T (2010) *Wolbachia* as a bacteriocyte-associated nutritional mutualist. *Proc Natl Acad Sci USA* 107:769–774.
15. Matsuura Y, et al. (2012) Evolution of symbiotic organs and endosymbionts in lygaeid stinkbugs. *ISME J* 6:397–409.
16. Koga R, Nikoh N, Matsuura Y, Meng XY, Fukatsu T (2013) Mealybugs with distinct endosymbiotic systems living on the same host plant. *FEMS Microbiol Ecol* 83:93–100.
17. Stoll S, Feldhaar H, Fraunholz MJ, Gross R (2010) Bacteriocyte dynamics during development of a holometabolous insect, the carpenter ant *Camponotus floridanus*. *BMC Microbiol* 10:308.
18. Perotti MA, Clarke HK, Turner BD, Braig HR (2006) *Rickettsia* as obligate and mycetomic bacteria. *FASEB J* 20:2372–2374.
19. Braendle C, et al. (2003) Developmental origin and evolution of bacteriocytes in the aphid-*Buchnera* symbiosis. *PLoS Biol* 1:E21.
20. Miura T, et al. (2003) A comparison of parthenogenetic and sexual embryogenesis of the pea aphid *Acyrthosiphon pisum* (Hemiptera: Aphidoidea). *J Exp Zoolog B Mol Dev Evol* 295:59–81.
21. Vigneron A, et al. (2014) Insects recycle endosymbionts when the benefit is over. *Curr Biol* 24:2267–2273.
22. Hansen AK, Moran NA (2011) Aphid genome expression reveals host-symbiont cooperation in the production of amino acids. *Proc Natl Acad Sci USA* 108:2849–2854.
23. Shigenobu S, Watanabe H, Hattori M, Sakaki Y, Ishikawa H (2000) Genome sequence of the endocellular bacterial symbiont of aphids *Buchnera* sp. APS. *Nature* 407:81–86.
24. International Aphid Genomics Consortium (2010) Genome sequence of the pea aphid *Acyrthosiphon pisum*. *PLoS Biol* 8:e1000313.
25. Simonet P, et al. (2016) Direct flow cytometry measurements reveal a fine-tuning of symbiotic cell dynamics according to the host developmental needs in aphid symbiosis. *Sci Rep* 6:19967.
26. Galluzzi L, et al. (2012) Molecular definitions of cell death subroutines: Recommendations of the nomenclature committee on cell death 2012. *Cell Death Differ* 19:107–120.
27. Fulda S, Kögel D (2015) Cell death by autophagy: Emerging molecular mechanisms and implications for cancer therapy. *Oncogene* 34:5105–5113.
28. Xie Z, Klionsky DJ (2007) Autophagosome formation: Core machinery and adaptations. *Nat Cell Biol* 9:1102–1109.
29. Yang Z, Klionsky DJ (2010) Mammalian autophagy: Core molecular machinery and signaling regulation. *Curr Opin Cell Biol* 22:124–131.
30. Levine B, Kroemer G (2008) Autophagy in the pathogenesis of disease. *Cell* 132:27–42.
31. Mizushima N, Levine B, Cuervo AM, Klionsky DJ (2008) Autophagy fights disease through cellular self-digestion. *Nature* 451:1069–1075.
32. Oropesa-Ávila M, et al. (2015) The apoptotic microtubule network during the execution phase of apoptosis. *Cell Death–Autophagy, Apoptosis and Necrosis*, ed Ntuli TM (InTech, Rijeka, Croatia), pp 299–329.
33. Park SH, Blackstone C (2010) Further assembly required: Construction and dynamics of the endoplasmic reticulum network. *EMBO Rep* 11:515–521.
34. Munro S, Pelham HR (1987) A C-terminal signal prevents secretion of luminal ER proteins. *Cell* 48:899–907.
35. Chavrier P, Parton RG, Hauri HP, Simons K, Zerial M (1990) Localization of low molecular weight GTP binding proteins to exocytic and endocytic compartments. *Cell* 62:317–329.
36. Fuchs Y, Steller H (2011) Programmed cell death in animal development and disease. *Cell* 147:742–758.
37. Sperandio S, de Belle I, Bredesen DE (2000) An alternative, nonapoptotic form of programmed cell death. *Proc Natl Acad Sci USA* 97:14376–14381.
38. Fuchs TA, et al. (2007) Novel cell death program leads to neutrophil extracellular traps. *J Cell Biol* 176:231–241.
39. Overholtzer M, et al. (2007) A nonapoptotic cell death process, entosis, that occurs by cell-in-cell invasion. *Cell* 131:966–979.
40. Andrabi SA, Dawson TM, Dawson VL (2008) Mitochondrial and nuclear cross talk in cell death: Parthanatos. *Ann N Y Acad Sci* 1147:233–241.
41. Bergsbaken T, Fink SL, Cookson BT (2009) Pyroptosis: Host cell death and inflammation. *Nat Rev Microbiol* 7:99–109.
42. Vandenabeele P, Galluzzi L, Vanden Berghe T, Kroemer G (2010) Molecular mechanisms of necroptosis: An ordered cellular explosion. *Nat Rev Mol Cell Biol* 11:700–714.
43. Overmeyer JH, Young AM, Bhanot H, Maltese WA (2011) A chalcone-related small molecule that induces methuosis, a novel form of non-apoptotic cell death, in glioblastoma cells. *Mol Cancer* 10:69.
44. Dixon SJ, et al. (2012) Ferroptosis: An iron-dependent form of nonapoptotic cell death. *Cell* 149:1060–1072.
45. Weerasinghe P, Buja LM (2012) Oncosis: An important non-apoptotic mode of cell death. *Exp Mol Pathol* 93:302–308.
46. Tait SWG, Ichim G, Green DR (2014) Die another way–Non-apototic mechanisms of cell death. *J Cell Sci* 127:2135–2144.
47. Montero J, Dutta C, van Bodegom D, Weinstock D, Letai A (2013) p53 regulates a non-apoptotic death induced by ROS. *Cell Death Differ* 20:1465–1474.
48. Yorimitsu T, Klionsky DJ (2007) Eating the endoplasmic reticulum: Quality control by autophagy. *Trends Cell Biol* 17:279–285.

49. Tooze SA, Yoshimori T (2010) The origin of the autophagosomal membrane. *Nat Cell Biol* 12:831–835.
50. Nakabachi A, et al. (2005) Transcriptome analysis of the aphid bacteriocyte, the symbiotic host cell that harbors an endocellular mutualistic bacterium, *Buchnera*. *Proc Natl Acad Sci USA* 102:5477–5482.
51. Chen MC, Cheng YM, Sung PJ, Kuo CE, Fang LS (2003) Molecular identification of Rab7 (ApRab7) in *Aiptasia pulchella* and its exclusion from phagosomes harboring zooxanthellae. *Biochem Biophys Res Commun* 308:586–595.
52. Chen MC, Cheng YM, Hong MC, Fang LS (2004) Molecular cloning of Rab5 (ApRab5) in *Aiptasia pulchella* and its retention in phagosomes harboring live zooxanthellae. *Biochem Biophys Res Commun* 324:1024–1033.
53. Hong MC, Huang YS, Lin WW, Fang LS, Chen MC (2009) ApRab3, a biosynthetic Rab protein, accumulates on the maturing phagosomes and symbiosomes in the tropical sea anemone, *Aiptasia pulchella*. *Comp Biochem Physiol B Biochem Mol Biol* 152: 249–259.
54. Mohamed AR, et al. (2016) The transcriptomic response of the coral *Acropora digitifera* to a competent *Symbiodinium* strain: The symbiosome as an arrested early phagosome. *Mol Ecol* 25:3127–3141.
55. Clayton AL, et al. (2012) A novel human-infection-derived bacterium provides insights into the evolutionary origins of mutualistic insect-bacterial symbioses. *PLoS Genet* 8: e1002990.
56. Voronin D, Cook DAN, Steven A, Taylor MJ (2012) Autophagy regulates Wolbachia populations across diverse symbiotic associations. *Proc Natl Acad Sci USA* 109: E1638–E1646.
57. Moran NA, Munson MA, Baumann P, Ishikawa H (1993) A molecular clock in endosymbiotic bacteria is calibrated using the insect hosts. *Proc R Soc B* 253:167–171.
58. Gil R, Sabater-Muñoz B, Latorre A, Silva FJ, Moya A (2002) Extreme genome reduction in *Buchnera* spp.: Toward the minimal genome needed for symbiotic life. *Proc Natl Acad Sci USA* 99:4454–4458.
59. Dale C, Moran NA (2006) Molecular interactions between bacterial symbionts and their hosts. *Cell* 126:453–465.
60. Coburn B, Sekirov I, Finlay BB (2007) Type III secretion systems and disease. *Clin Microbiol Rev* 20:535–549.
61. Escoll P, Mondino S, Rolando M, Buchrieser C (2016) Targeting of host organelles by pathogenic bacteria: A sophisticated subversion strategy. *Nat Rev Microbiol* 14:5–19.
62. Shigenobu S, Stern DL (2013) Aphids evolved novel secreted proteins for symbiosis with bacterial endosymbiont. *Proc Biol Sci* 280:20121952.
63. Peccoud J, et al. (2014) Inheritance patterns of secondary symbionts during sexual reproduction of pea aphid biotypes. *Insect Sci* 21:291–300.
64. Hara E, Fukatsu T, Ishikawa H (1990) Characterisation of symbionin with anti-symbionin antiserum. *Insect Biochem* 20:429–436.
65. Sapountzis P, et al. (2014) New insight into the RNA interference response against cathepsin-L gene in the pea aphid, *Acyrthosiphon pisum*: Molting or gut phenotypes specifically induced by injection or feeding treatments. *Insect Biochem Mol Biol* 51: 20–32.
66. Clements J, Hens K, Francis C, Schellens A, Callaerts P (2008) Conserved role for the *Drosophila* Pax6 homolog eyeless in differentiation and function of insulin-producing neurons. *Proc Natl Acad Sci USA* 105:16183–16188.
67. Schneider CA, Rasband WS, Eliceiri KW (2012) NIH image to ImageJ: 25 years of image analysis. *Nat Methods* 9:671–675.
68. Mangano S, et al. (2017) Molecular link between auxin and ROS-mediated polar growth. *Proc Natl Acad Sci USA* 114:5289–5294.
69. Pfaffl MW, Tichopad A, Prgomet C, Neuvians TP (2004) Determination of stable housekeeping genes, differentially regulated target genes and sample integrity: BestKeeper–Excel-based tool using pair-wise correlations. *Biotechnol Lett* 26:509–515.
70. Legeai F, et al. (2010) AphidBase: A centralized bioinformatic resource for annotation of the pea aphid genome. *Insect Mol Biol* 19:5–12.